Supplementary Information: *Ultrabroadband Integrated Electro-Optic Frequency Comb in Lithium Tantalate*

Junyin Zhang,[1,2,*] Chengli Wang,[1,2,*] Connor Denney,[3,*] Johann Riemensberger,[1,2,*] Grigory Lihachev,[1,2] Jianqi Hu,[1,2] Wil Kao,[1,2] Terence Blésin,[1,2] Nikolai Kuznetsov,[1,2] Zihan Li,[1,2] Mikhail Churaev,[1,2] Xin Ou,[4,†] Gabriel Santamaria-Botello,[3,‡] and Tobias J. Kippenberg[1,2,§]

[1]*Institute of Physics, Swiss Federal Institute of Technology Lausanne (EPFL), CH-1015 Lausanne, Switzerland*
[2]*Center of Quantum Science and Engineering, EPFL, CH-1015 Lausanne, Switzerland*
[3]*Departement of Electrical Engineering, Colorado School of Mines, Golden, Colorado 80401, United States*
[4]*State Key Laboratory of Materials for Integrated Circuits, Shanghai Institute of Microsystem and Information Technology, Chinese Academy of Sciences, Shanghai, China*

CONTENTS

* These authors contributed equally.
† ouxin@mail.sim.ac.cn
‡ gabriel.santamariabotello@mines.edu
§ tobias.kippenberg@epfl.ch

I. CAVITY ELECTRO-OPTICS AND COMB GENERATION

A. Hamiltonian formalism

The Pockels effect drives frequency conversion processes in the lithium tantalate ($LiTaO_3$) microresonator forming the comb generator. It alters the optical permeability $\eta = 1/\epsilon_r$ in response to a microwave electric field E^{m} such that

$$\Delta\eta_{ij} = r_{ijk}E^{\mathrm{m}}_k, \tag{1}$$

where r_{ijk} and ϵ_r denote the Pockels tensor components and relative permittivity, respectively. Here we use the Einstein notation. According to Bethe–Schwinger perturbation theory for cavities [1], the change in optical impermeability, in turn, implies a change in the refractive index n

$$\Delta n = \frac{n}{2\epsilon_0}\frac{\iiint D_i^{\mathrm{opt}}\Delta\eta_{ij}D_j^{\mathrm{opt}}\,d\mathcal{V}}{\iiint E_i^{\mathrm{opt}}\epsilon_{ij}E_j^{\mathrm{opt}}\,d\mathcal{V}}, \tag{2}$$

where D_i^{opt} and E_i^{opt} correspond to the optical electric displacement and field components, and ϵ_0 and ϵ_{ij} denote the vacuum permittivity and the permittivity tensor components at optical frequencies. Consider first just one single optical cavity mode. The modification of the optical path length of the cavity then leads to a shift in its resonance frequency. The parametric dependence of the resonance frequency on E^{m} is encapsulated in the interaction Hamiltonian

$$\hat{\mathcal{H}}^{\mathrm{EO}} = -\frac{1}{\tau}\hbar\hat{\phi}\hat{a}^\dagger\hat{a}, \tag{3}$$

where $\hat{a}$ and $\hat{a}^\dagger$ are the annihilation and creation operators of the optical field, $\hbar$ is the reduced Planck constant, τ is the round trip time of the optical cavity, and $\hat{\phi}$ is the optical phase delay in response to the microwave field [2]. By introducing a microwave resonator in the realization of a cavity electro-optic system [2, 3], we have

$$\hat{\phi} = \frac{2\pi m}{n}\frac{\partial n}{\partial V}V_{\mathrm{ZPF}}\left(\hat{b}+\hat{b}^\dagger\right) \tag{4}$$

for the m^{th}-harmonic optical mode. Here, $\hat{b}$ and $\hat{b}^\dagger$ are the annihilation and creation operators of the microwave mode. The corresponding zero-point voltage $V_{\mathrm{ZPF}} = \sqrt{\hbar\omega_{\mathrm{m}}/(2C)}$, which increases (decreases) with the microwave resonance frequency ω_m (the capacitance C). Combining Eqs. (3) and (4), we obtain an interaction Hamiltonian that takes on the same form as the canonical two-mode optomechanical Hamiltonian

$$\hat{\mathcal{H}}^{\mathrm{EO}} = -\hbar g_0'\hat{a}^\dagger\hat{a}\left(\hat{b}+\hat{b}^\dagger\right). \tag{5}$$

For cavity electro-optics, the vacuum coupling rate

$$g_0' = \frac{1}{\tau}\frac{2\pi m}{n}\frac{\partial n}{\partial V}V_{\mathrm{ZPF}} \tag{6}$$

can be interpreted as the frequency shift of the optical mode induced by a single microwave photon. Consider instead a triply resonant system with two optical modes ($\hat{a}_1$, $\hat{a}_2$) and one microwave mode ($\hat{b}$). Equations (2) and (5) can be extended as

$$\begin{aligned}\hat{\mathcal{H}}^{\mathrm{EO}} =& -\hbar g_0'\left(\hat{a}_1^\dagger\hat{a}_1+\hat{a}_2^\dagger\hat{a}_2\right)\left(\hat{b}+\hat{b}^\dagger\right)\\ &-\hbar g_0\left(\hat{a}_1^\dagger\hat{a}_2+\hat{a}_1\hat{a}_2^\dagger\right)\left(\hat{b}+\hat{b}^\dagger\right),\end{aligned} \tag{7}$$

where both self- and cross-mode couplings are included through g_0' and g_0 respectively. EO comb generation concerns cross-mode coupling involving $\hat{a}_1$, $\hat{a}_2$, and $\hat{b}$.

Besides comb generation, it is interesting to point out that cavity electro-optics can be leveraged for quantum coherent microwave-optical transduction. With a large coherent drive of amplitude α inside the optical cavity (assumed to be a real number without loss of generality), the two-mode interaction Hamiltonian (Eq. (5)) can be linearized as

$$\begin{aligned}\hat{\tilde{\mathcal{H}}}^{\mathrm{EO}} &= -\hbar g_0'\alpha\left(\hat{a}+\hat{a}^\dagger\right)\left(\hat{b}+\hat{b}^\dagger\right)\\ &= -\hbar g_0'\alpha\left(\hat{a}\hat{b}^\dagger+\hat{a}^\dagger\hat{b}\right)-\hbar g_0'\alpha\left(\hat{a}\hat{b}+\hat{a}^\dagger\hat{b}^\dagger\right).\end{aligned} \tag{8}$$

The two terms mediate quantum state transfer and two-mode squeezing between the optical and microwave modes, respectively [4]. The effective coupling rate ($g_0'\alpha$) is enhanced by the intracavity pump field.

B. Comb generation

The comb generator operates in the regime where the free spectral range (FSR) $\omega_{\mathrm{FSR}} = 2\pi/\tau = 2\pi f_{\mathrm{FSR}}$ is close to the resonance frequency of the microwave cavity ω_{m}. This leads to cascaded interactions between optical modes mediated by the microwave

$$\hat{\mathcal{H}}^{\mathrm{EO}} = \sum_{\mu} -\hbar g_0 \left(\hat{a}_{\mu+1} \hat{a}_{\mu}^{\dagger} \hat{b}^{\dagger} + \hat{a}_{\mu}^{\dagger} \hat{a}_{\mu-1} \hat{b} \right), \tag{9}$$

where the cross-coupling terms from Eq. (7) satisfying $\omega_{\mu+1} = \omega_{\mu} + \omega_{\mathrm{m}}$ is included. For simplicity, the vacuum coupling rate is assumed to be constant over the comb span. The full system Hamiltonian with an optical drive and a microwave pump at frequencies ω_{L} (close to mode $\mu = \mu'$) and ω_{D} is given by

$$\begin{aligned} \hat{\mathcal{H}} &= \hbar\omega_{\mathrm{m}} \hat{b}^{\dagger}\hat{b} + \sum_{\mu} \hbar\omega_{\mu} \hat{a}_{\mu}^{\dagger}\hat{a}_{\mu} + \hat{\mathcal{H}}^{\mathrm{EO}} \\ &+ i\hbar\sqrt{\kappa_{\mathrm{ex},\mu'}} \left(\hat{a}_{\mathrm{in}} \hat{a}_{\mu'}^{\dagger} e^{-i\omega_{\mathrm{L}} t} - \hat{a}_{\mathrm{in}}^{\dagger} \hat{a}_{\mu'} e^{i\omega_{\mathrm{L}} t} \right) + i\hbar\sqrt{\kappa_{\mathrm{ex,m}}} \left(\hat{b}_{\mathrm{in}} \hat{b}^{\dagger} e^{-i\omega_{\mathrm{D}} t} - \hat{b}_{\mathrm{in}}^{\dagger} \hat{b} e^{i\omega_{\mathrm{D}} t} \right). \end{aligned} \tag{10}$$

For ease of physical interpretation, we go into the frame co-rotating with microwave drive frequency ω_{D} for $\hat{b}$ and the evenly spaced optical frequency grid centered on the laser frequency $\omega_{\mathrm{L}} + (\mu - \mu')\, D_1$ for $\{\hat{a}_{\mu}\}$. The associated input laser and microwave pump detunings are in turn denoted as $\Delta_{\mathrm{L}} = \omega_{\mathrm{L}} - \omega_{\mu'}$ and $\Delta_{\mathrm{m}} = \omega_{\mathrm{D}} - \omega_{\mathrm{m}}$, respectively. Moreover, D_1 is the optical FSR defined with respect to the driven mode μ'. The optical gross detuning, defined in the main text as $\Delta_{\mu} = \Delta_{\mathrm{L}} - D_{\mathrm{int}}(\mu)$, is encapsulated in the self-energy term of the Hamiltonian in this frame. Here, we account for the integrated dispersion $D_{\mathrm{int}}(\mu) = \omega_{\mu} - [\omega_{\mu'} + (\mu - \mu')D_1]$. Setting $\mu' = 0$, we therefore have

$$\begin{aligned} \hat{\mathcal{H}} = -\hbar\Delta_{\mathrm{m}} \hat{b}^{\dagger}\hat{b} - \sum_{\mu} \hbar\Delta_{\mu} \hat{a}_{\mu}^{\dagger}\hat{a}_{\mu} - \sum_{\mu} \hbar g_0 \left(\hat{a}_{\mu+1} \hat{a}_{\mu}^{\dagger} \hat{b}^{\dagger} e^{-i(D_1 - \omega_{\mathrm{D}})t} + \hat{a}_{\mu}^{\dagger} \hat{a}_{\mu-1} \hat{b} e^{i(D_1 - \omega_{\mathrm{D}})t} \right) \\ + i\hbar\sqrt{\kappa_{\mathrm{ex},0}} \left(\hat{a}_{\mathrm{in}} \hat{a}_0^{\dagger} - \hat{a}_{\mathrm{in}}^{\dagger} \hat{a}_0 \right) + i\hbar\sqrt{\kappa_{\mathrm{ex,m}}} \left(\hat{b}_{\mathrm{in}} \hat{b}^{\dagger} - \hat{b}_{\mathrm{in}}^{\dagger} \hat{b} \right), \end{aligned} \tag{11}$$

Since we choose $\omega_{\mathrm{D}} = D_1$, the time dependence from the phase term in the first line drops off. The internal system dynamics can then be obtained using the Heisenberg equations $\frac{d}{dt}\hat{a}_{\mu} = \frac{1}{i\hbar}\left[\hat{a}_{\mu}, \hat{\mathcal{H}}\right] + \frac{\partial \hat{a}_{\mu}}{\partial t}$

$$\begin{aligned} \frac{d}{dt}\hat{a}_{\mu}(t) &= \left[i\Delta_{\mu} - \frac{\kappa_{\mu}}{2} \right] \hat{a}_{\mu}(t) + ig_0 \hat{a}_{\mu+1}(t)\hat{b}^{\dagger}(t) + ig_0 \hat{a}_{\mu-1}(t)\hat{b}(t) + \sqrt{\kappa_{\mathrm{ex},0}}\hat{a}_{\mathrm{in}}(t)\delta_{\mu,0}, \\ \frac{d}{dt}\hat{b}(t) &= \left[i\Delta_{\mathrm{m}} - \frac{\kappa_{\mathrm{m}}}{2} \right] \hat{b}(t) + \sum_{\mu} ig_0 \hat{a}_{\mu+1}(t)\hat{a}_{\mu}^{\dagger}(t) + \sqrt{\kappa_{\mathrm{ex,m}}}\hat{b}_{\mathrm{in}}(t), \end{aligned} \tag{12}$$

where $\kappa_{\mathrm{ex},\mu}$ and $\kappa_{\mathrm{ex,m}}$ (κ_{μ} and κ_{m}) represent the external coupling (total decay) rates of the modes, and $\delta_{\mu,0}$ is the Kronecker delta function. With a strong microwave pump with power P_{D} and phase ϕ_{D}, the microwave equation of motion can be simplified by dropping the coupling terms with the optical modes as

$$\frac{d}{dt}\hat{b}(t) \approx \left[i\Delta_{\mathrm{m}} - \frac{\kappa_{\mathrm{m}}}{2} \right] \hat{b}(t) + \sqrt{\kappa_{\mathrm{ex,m}}}\hat{b}_{\mathrm{in}}(t). \tag{13}$$

Without loss of generality, we set $\phi_{\mathrm{D}} = 0$. The microwave photons mediate the interaction between the optical modes. The steady-state mean intracavity microwave photon number can be computed as

$$n_{\mathrm{m}} = \frac{\kappa_{\mathrm{ex,m}}}{\Delta_{\mathrm{m}}^2 + \kappa_{\mathrm{m}}^2/4} \frac{P_{\mathrm{D}}}{\hbar\omega_{\mathrm{D}}}, \tag{14}$$

and the effective EO coupling rate becomes $g = g_0\sqrt{n_{\mathrm{m}}}$.

Following Eq. (12) and neglecting vacuum fluctuations, we can write the coupled mode equations describing the dynamics of the slowly varying electric field amplitudes $a_{\mu}(t) = \langle \hat{a}_{\mu}(t) \rangle$, given by

$$\frac{d}{dt}a_{\mu}(t) = \left[i\Delta_{\mu} - \frac{\kappa_{\mu}}{2} \right] a_{\mu}(t) + ig\left[a_{\mu-1}(t) + a_{\mu+1}(t) \right] + \sqrt{\kappa_{\mathrm{ex}}}a_{\mathrm{in}}(t)\delta_{\mu,0}. \tag{15}$$

In the presence of strong birefringence-induced mode-mixing between TE and TM modes, D_{int} can no longer be described by a polynomial series. The resonances become locally shifted.

C. Comb slope and span

The comb envelope slope can then be derived from Eq. (15). Assuming $\Delta_\mu \approx 0$, we have

$$\frac{d}{dt}a_\mu(t) = -\frac{\kappa_\mu}{2}a_\mu + ig\left(a_{\mu-1} + a_{\mu+1}\right) = 0. \tag{16}$$

in the steady state. For simplicity, let all $\kappa_\mu = \kappa$. Assuming a constant slope for the comb envelope, i.e., $\hat{a}_{\mu+1}/\hat{a}_\mu = \lambda$ for $\mu > 0$ and $\hat{a}_{\mu-1}/\hat{a}_\mu = \lambda$ for $\mu < 0$, we obtain

$$-\frac{\kappa}{2} + ig\left(\frac{1}{\lambda} + \lambda\right) = 0. \tag{17}$$

In the regime of strong EO interaction where $g \gg \kappa$, the solution of λ reads

$$\lambda = -i\left(\frac{\kappa}{4g} - \sqrt{1 + \left(\frac{\kappa}{4g}\right)^2}\right) \approx i\left(1 - \frac{\kappa}{4g}\right) \approx i\exp\left(-\frac{\kappa}{4g}\right). \tag{18}$$

The power ratio between adjacent comb lines (for $\mu > 0$) is therefore given by

$$\frac{P_{\mu+1}}{P_\mu} = |\lambda|^2 \approx \exp\left(-\frac{\kappa}{2g}\right). \tag{19}$$

D. Birefringence Limit

In this section, we derive the comb power drop when the dispersion contribution of the gross detuning Δ_μ is no longer negligible. As discussed in the main text, birefringence-induced mode-mixing is one major reason for such resonance frequency shift in e.g., $LiNbO_3$, imposing limits on the attainable comb span. When mode-mixing occurs at mode $\mu = \mu_0 > 0$, the induced resonance frequency distortion δ_{μ_0} can be at the gigahertz level, which is much larger than the typical cavity loss rate κ. Consequently, we can omit the loss term in Eq. (15) and obtain the steady-state field amplitude as

$$\frac{d}{dt}a_{\mu_0}(t) = i\Delta_{\mu_0}a_{\mu_0}(t) + ig\left[a_{\mu_0-1}(t) + a_{\mu_0+1}(t)\right] = 0. \tag{20}$$

Since the resonance distortion induces a significant drop in the comb line field amplitude, given as

$$a_{\mu_0-1} \gg a_{\mu_0+1}, \tag{21}$$

we can approximate Eq. (20) as

$$i\Delta_{\mu_0}a_{\mu_0} + iga_{\mu_0-1} = 0. \tag{22}$$

The power drop at the mode-mixing point μ_0 is therefore

$$\frac{P_{\mu_0}}{P_{\mu_0-1}} = \left|\frac{a_{\mu_0}}{a_{\mu_0+1}}\right|^2 = \left|\frac{g}{\Delta_{\mu_0}}\right|^2. \tag{23}$$

When mode-mixing occurs, several nearby modes typically become distorted. Additionally, the effective EO coupling rate will decrease from g to g_{μ_0}, since the hybrid mode does not fully utilize $\chi^{(2)}_{333}$ of $LiTaO_3$, unlike the TE mode. The combined effect thus leads to a cascaded power drop as

$$\frac{P_{\mu_0+N}}{P_{\mu_0}} \approx \prod_{j=0}^{N-1}\frac{P_{\mu_0+j+1}}{P_{\mu_0+j}} \approx \left|\prod_{j=0}^{N-1}\frac{g_{\mu_0+j+1}}{\Delta_{\mu_0+j+1}}\right|^2, \tag{24}$$

for a mode N FSRs away.

E. Comb existence range

In this section, we discuss the comb existence range as a function of laser detuning, which is directly related to the stability of the comb when the input laser frequency fluctuates. In Eq. (15), omitting the κ term for all modes as well as integrated dispersion $D_{\mathrm{int}}(\mu)$ such that $\Delta_\mu = \Delta_{\mathrm{L}}$, we have

$$\frac{d}{dt}a_\mu(t) = i\Delta_{\mathrm{L}}a_\mu + ig\left(a_{\mu-1} + a_{\mu+1}\right) = 0. \tag{25}$$

Following the constant comb slope assumption as in Section I C, we obtain from Eq. (25)

$$i\Delta_{\mathrm{L}} + ig\left(\frac{1}{\lambda} + \lambda\right) = 0. \tag{26}$$

Choosing the solution on physical grounds for $\mu > 0$, we have

$$\lambda = \frac{1}{2}\left(\frac{\Delta_{\mathrm{L}}}{g} - \sqrt{\left(\frac{\Delta_{\mathrm{L}}}{g}\right)^2 - 4}\right). \tag{27}$$

As the comb slope λ decrease significantly when $\left(\Delta_{\mathrm{L}}/g\right)^2 - 4 > 0$, the comb cut-off occurs at the detuning

$$|\Delta_{\mathrm{L}}| > 2g. \tag{28}$$

It can be seen that enhancing g with a microwave resonator extends the comb existence range, approaching the optical resonator FSR in our case. The expression for the normalized comb slope $P_{\mu+1}/P_\mu = |\lambda|^2$ when $\kappa \neq 0$ can be derived using the same method. The numerical simulation results are shown in Figure S1. In our triply resonant system, with 37-dBm on-chip microwave power, we have $\kappa/g \approx 0.013$.

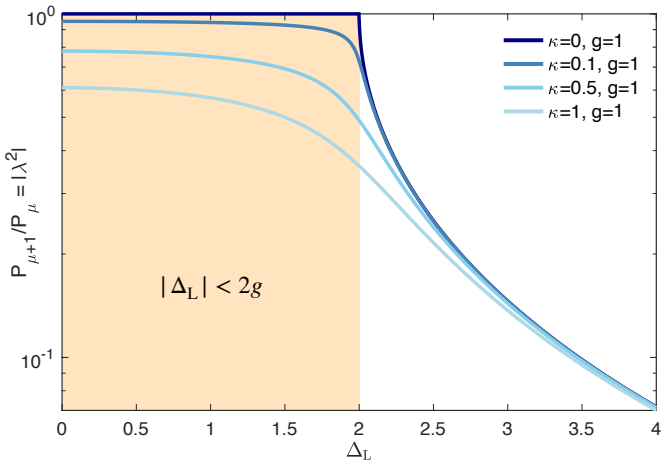

Figure S1. Normalized comb slope $P_{\mu+1}/P_\mu$ from simulation, with the same normalized coupling rate g and different cavity loss rates κ. The comb existence range is given by $|\Delta_{\mathrm{L}}| < 2g$. In the ideal case when $g \gg \kappa$, the comb slope remains unchanged within the range. The comb slope undergoes a sharp decline when $\Delta_{\mathrm{L}} = \pm 2g$. This cut-off becomes less sharp as the cavity linewidth κ increases.

F. Analytic solution and pulse width

In this section, we derive the rigorous analytical solution for the comb equation Eq. (15) in steady state. Utilizing this analytical solution, we subsequently derive the pulse width in the time domain for the EO comb. In steady state, we have

$$\frac{\mathrm{d}a_\mu}{\mathrm{d}t} = \left(-\frac{\kappa}{2} + i\Delta_\mu\right)a_\mu + ig\left(a_{\mu-1} + a_{\mu+1}\right) + \sqrt{\kappa_{\mathrm{ex}}}a_{\mathrm{in}}\delta_{\mu,0} = 0. \tag{29}$$

Here $\mu = -N/2, \cdots, N/2$, with $N \to +\infty$ being the total number of modes. Introducing a new basis in the Fourier domain, we define

$$A_k = \frac{1}{\sqrt{N}} \sum_\mu a_\mu e^{\frac{2\pi i}{N}\mu k} \tag{30}$$

so that $a_\mu = \frac{1}{\sqrt{N}} \sum_k A_k e^{\frac{-2\pi i}{N}\mu k}$. Omitting dispersion such that $\Delta_\mu = \Delta_\mathrm{L}$ and rewriting Eq. (29) with A_k, we have

$$\left(-\frac{\kappa}{2} + i\Delta_\mathrm{L}\right) A_k + 2ig\cos\left(\frac{2\pi k}{N}\right) A_k + \sqrt{\frac{\kappa_\mathrm{ex}}{N}} a_\mathrm{in} = 0, \tag{31}$$

where

$$A_k = \sqrt{\frac{\kappa_\mathrm{ex}}{N}} \frac{1}{(\kappa/2 - i\Delta_\mathrm{L}) - 2ig\cos(2\pi k/N)} a_\mathrm{in}. \tag{32}$$

Using Eq. (30) and taking the limit $N \to +\infty$, we have

$$\begin{aligned} a_\mu &= \sqrt{\kappa_\mathrm{ex}} \sum_k \frac{1}{(\kappa/2 - i\Delta_\mathrm{L}) - 2ig\cos(2\pi k/N)} e^{-\frac{2\pi i}{N}\mu k} a_\mathrm{in} \\ &= \sqrt{\kappa_\mathrm{ex}} \int_{-\pi}^{\pi} \frac{\mathrm{d}u}{2\pi} \frac{1}{(\kappa/2 - i\Delta_\mathrm{L}) - 2ig\cos u} e^{-i\mu u} a_\mathrm{in}\Big|_{u=2\pi k/N} \\ &= \sqrt{\kappa_\mathrm{ex}} \oint_{|z|=1} \frac{\mathrm{d}z}{2\pi i} \frac{1}{z} \frac{z^\mu}{(\kappa/2 - i\Delta_\mathrm{L}) - ig(z + 1/z)} a_\mathrm{in}\Big|_{z=e^{-iu}}. \end{aligned} \tag{33}$$

We found the contour integral can be calculated by the residue theorem as

$$a_\mu = \frac{i\sqrt{\kappa_\mathrm{ex}}\, z_0^\mu}{\sqrt{(\Delta_\mathrm{L} - i\kappa/2)^2 - 4g^2}} a_\mathrm{in}, \tag{34}$$

where z_0 is the solution for $(\kappa/2 - i\Delta_\mathrm{L})z - ig(z + 1/z)z = 0$ within $|z| < 1$ for $\mu > 0$ (the solution outside $|z| > 1$ for $\mu < 0$). The solution provided in Eq. (34) confirms the validity of the ansatz used earlier in Section I C, where $a_{\mu+1}/a_\mu = z_0$. Additionally, the splitting of the resonance in the optical transmission is also evident from Eq. (34), as it occurs when $\Delta_\mathrm{L}^2 - 4g^2 = 0$.

Now we consider the pulse in the time domain. The Fourier domain introduced previously for A_k in Eq. (30) is actually the physical time. The optical field inside the optical cavity at time t is given by

$$a(t) = \sum_\mu a_\mu e^{i\mu\omega_\mathrm{FSR} t}. \tag{35}$$

Here, ω_FSR corresponds to the optical FSR, which is related to the comb repetition rate by $\omega_\mathrm{FSR} = 2\pi f_\mathrm{rep}$. Comparing with Eq. (30), we have

$$a(t) = \sqrt{N} A_k, \tag{36}$$

where $k = \omega_\mathrm{FSR} t N/(2\pi)$. With Eq. (32), the pulse of EO comb in the time domain can be written as:

$$a(t) = \frac{\sqrt{\kappa_\mathrm{ex}}}{(\kappa/2 - i\Delta_\mathrm{L}) - 2ig\cos\omega_\mathrm{FSR} t}. \tag{37}$$

The pulse power $I(t) = |a(t)|^2$ when $\Delta_\mathrm{L} = 0$ is

$$I(t) \propto \frac{1}{\kappa^2 + 16g^2\cos^2\omega_\mathrm{FSR} t}, \tag{38}$$

from which we obtain the pulse full width at half maximum

$$\Delta t = \frac{\kappa}{2g\omega_\mathrm{FSR}}. \tag{39}$$

In our system with $\kappa/(2\pi) = 100\,\mathrm{MHz}$, $g/(2\pi) = 7.5\,\mathrm{GHz}$, and $\omega_\mathrm{FSR}/(2\pi) = 30\,\mathrm{GHz}$, we obtain the pulse width $\Delta t = 35\,\mathrm{fs}$.

G. Numerical simulations of comb span and existence range

The steady-state solution of the system is found trivially by setting $da_\mu/dt = 0$ and inverting Eq. (15). Because we operate the triply resonant system in a regime where the effective EO coupling rate $g = 2\pi \times 7.5\,\mathrm{GHz}$ is comparable to the optical microresonator FSR, we have to include the coupling of the laser to multiple longitudinal modes in the optical microresonator. This regime mandates the use of an explicit time-domain model (Ikeda map) of the field propagation inside the racetrack resonator for the simulation of nonlinear frequency comb generation. For the linear system of the EO comb, we can simply calculate the comb generation for all the resonator modes close to the pump separately and coherently add the generated sideband amplitudes to capture the mutual interferences of the combs generated by coupling the laser field into multiple resonator modes, given by

$$a_\mu = \sum_{\nu=-3..3} \frac{ig\left(a_{\mu-1} + a_{\mu+1}\right) + \sqrt{\kappa_{\mathrm{ex}}} a_{\mathrm{in}} \delta_{\mu,\nu}}{-\kappa/2 + i\Delta_\mu - i\nu D_1}. \tag{40}$$

Figure S2 depicts a calculation of the generated combs inside the racetrack resonator and in the bus waveguide for an FSR $D_1/(2\pi)$ of 30 GHz, internal $\kappa_0/(2\pi)$ and external $\kappa_{\mathrm{ex}}/(2\pi)$ photon decay rates of 30 MHz, a mismatch between the optical FSR and the microwave pump $(D_1 - \omega_{\mathrm{D}})/(2\pi)$ of 2 MHz, and a small normal dispersion $D_2/(2\pi)$ of 2 kHz for an integrated dispersion of $D_{\mathrm{int}} = D_2/2 \times \mu^2$. Plotting the resulting output power spectrum in Fig. S2a and S2d, we find excellent agreement with the observed detuning spectrogram depicted in Fig. 4 of the main manuscript. If the laser is tuned to the center between two resonances, we observe a destructive interference between the generated sidebands at a high offset frequency with a slight tilt that is related to the small microwave detuning. Figure S2c and S2f depict the change in comb sideband powers as we tune the laser over a full FSR. We find that at an intermediate optical frequency offset of 10 THz, the comb sideband stays almost constant, and in general, we can tune the laser by more than 15 GHz with only a 1.5 dB sideband modulation amplitude.

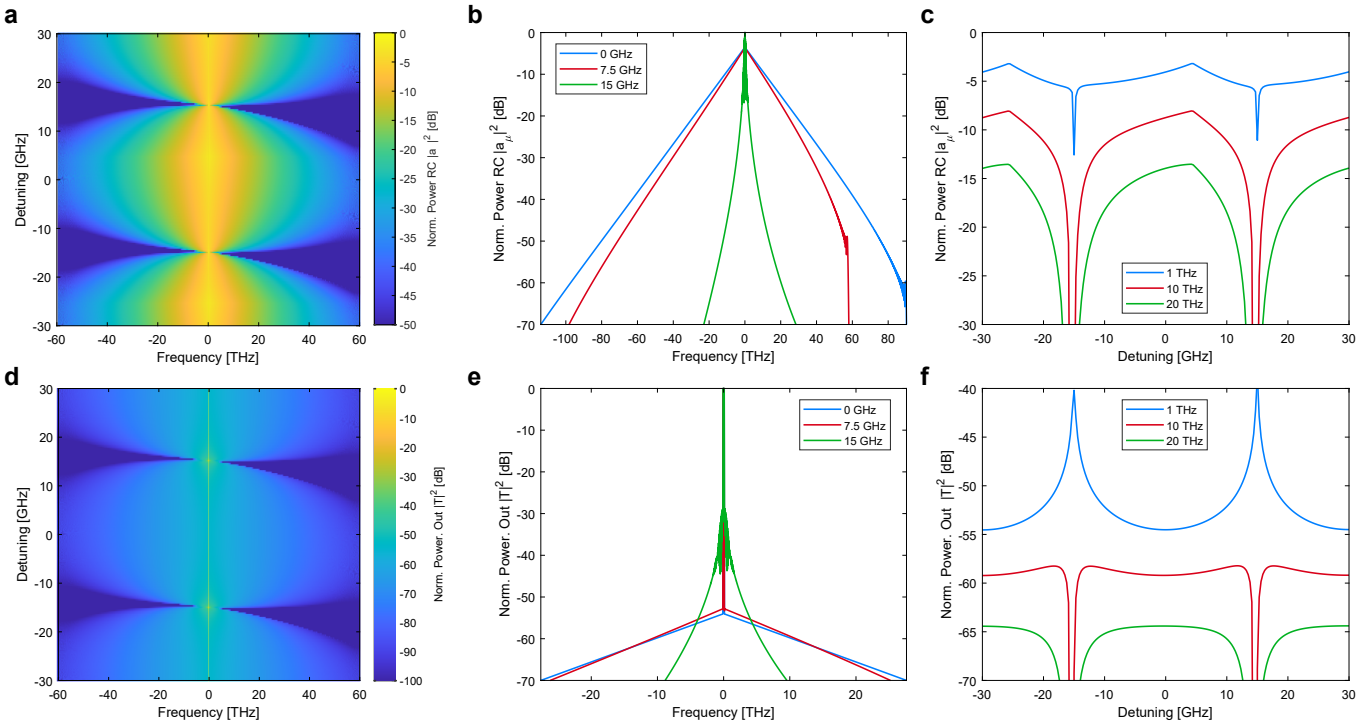

Figure S2. **Numerical simulation of comb span and existence.** (a) Normalized spectrogram of intracavity optical power $|a_\mu|^2$ as function of laser cavity detuning Δ_{L} at a microwave-FSR mismatch of $(D_1 - \omega_{\mathrm{D}})/(2\pi) = 2\,\mathrm{MHz}$. (b) Optical spectra at three different detunings, 0 GHz (blue), 7.5 GHz (red), 15 GHz (green). (c) Comb line power as a function of detuning for comb lines at 1 THz (blue), 10 THz (red), 20 THz (green) positive offset from the pump laser frequency. (d,e,f) Same as (a,b,c) but for outcoupled power in the optical bus waveguide.

II. MICROWAVE ENGINEERING FOR ELECTRO-OPTIC FREQUENCY COMB GENERATION

A. Definitions

The span of a triply resonant EO comb scales with $\sqrt{\mathcal{C}}$, where the cooperativity $\mathcal{C} = 4g_0^2 n_\mathrm{m}/\kappa^2$. Equivalently defined as in Eq. (14),

$$n_\mathrm{m} = \frac{4P_\mathrm{m}}{\hbar\omega_\mathrm{m}^2} Q_{\mathrm{m},0}\eta(1-\eta) \tag{41}$$

represents the microwave intracavity photon number, where P_m and ω_m denote the input microwave power and frequency, respectively. The coupling efficiency $\eta = Q_{\mathrm{m},0}/(Q_{\mathrm{m},0} + Q_{\mathrm{m,ex}})$ is related to its intrinsic and external quality factors ($Q_{\mathrm{m},0}$ and $Q_{\mathrm{m,ex}}$, respectively). The intrinsic and external loss rates of the optical modes are denoted as κ_0 and κ_ex, respectively. The total optical cavity loss rate is therefore $\kappa = \kappa_0 + \kappa_\mathrm{ex}$. The cross-mode vacuum coupling rate in Eq. (9) can be computed as

$$g_0 = \frac{\varepsilon_0}{4}\sqrt{\frac{\hbar\omega_\mathrm{m}\omega_\mathrm{p}\omega_\mathrm{s}}{W_\mathrm{m}W_\mathrm{p}W_\mathrm{s}}}\int_{\mathrm{LiTaO_3}} \chi^{(2)}_{ijk} E_{\mathrm{p},i} E^*_{\mathrm{s},j} E_{\mathrm{m},k}\,\mathrm{d}V. \tag{42}$$

The three-wave mixing process here involves a microwave pump field $\mathbf{E}_\mathrm{m}$ of frequency ω_m, mediating interaction between two optical modes ($\mathbf{E}_{\mathrm{p,s}}$) such that $\omega_\mathrm{s} = \omega_\mathrm{p} \pm \omega_\mathrm{m}$. The mode fields are normalized to their respective energies using

$$W_{\mathrm{m,p,s}} = \frac{\varepsilon_0}{2}\int \varepsilon_r(\omega_{\mathrm{m,p,s}})|\mathbf{E}_{\mathrm{m,p,s}}|^2\,\mathrm{d}V, \tag{43}$$

where $\varepsilon_r(\omega_{\mathrm{m,p,s}})$ is the space-dependent relative permittivity of the medium at the corresponding mode frequency.

B. Microwave resonator design

Three parameters can be controlled from a microwave engineering standpoint to maximize $\mathcal{C}$ and thus, the comb span, for a given P_m: (i) the overlap integral of the vacuum coupling rate, which must be maximized via the engineering of the field distribution, (ii) the external quality factor $Q_{\mathrm{m,ex}} = Q_{\mathrm{m},0}$ for critical coupling and maximization of n_m, and (iii) the microwave intrinsic quality factor $Q_{\mathrm{m},0}$ which shall be maximized.

1. *Maximize g_0 with optimal microwave field distribution*

We focus our study on racetrack resonators where the straight arms of length ℓ_s are orthogonal to the optical axis of the crystal ($\hat{c} = \pm\hat{z}$), as depicted in Fig. S3. A given coplanar waveguide (CPW)-like microwave field distribution permeates the straight arms, and no microwave field exists in the bent arms of arc length ℓ_b. A longitudinal coordinate ℓ is defined along the entire perimeter of the racetrack resonator.

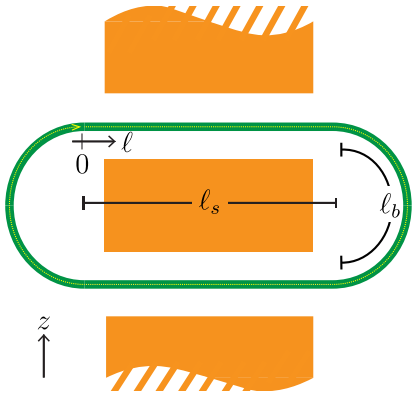

Figure S3. Schematic of racetrack resonator embedded in coplanar waveguide (CPW).

The overlap integral in Eq. (42) is computed inside the optical waveguide and within the straight sections only, where $\chi^{(2)} \neq 0$ and $|\mathbf{E}_\mathrm{m}| = E_\mathrm{m} \neq 0$. In this region, we assume the fields are separable in the transversal and longitudinal coordinates, i.e., $\mathbf{E}_\mathrm{m} = \mathbf{\Psi}_\mathrm{m}(\mathbf{r}_\perp) f_\mathrm{m}(\ell)$, and $\mathbf{E}_\mathrm{p,s} = \mathbf{\Psi}_\mathrm{p,s}(\mathbf{r}_\perp) e^{-i\beta_\mathrm{p,s}\ell}$, where β_p, and β_s are the wavenumbers of the pump and sideband, respectively, and $\int_V \mathrm{d}V \equiv \int_S \int_\ell \mathrm{d}\ell\,\mathrm{d}S$. Then, owing to the similarity between transversal profiles of pump and sideband modes, we consider the $\mathbf{\Psi}_\mathrm{p}$ only, and the expression for the vacuum coupling rate reduces to $g_0 = K \times \zeta \times \Delta S^{-1/2} \times I$. Aside from the pre-factor

$$K = \chi^{(2)} \left(\frac{\hbar \omega_\mathrm{m} \omega_\mathrm{p} \omega_\mathrm{s}}{2\varepsilon_0 \varepsilon_r(\omega_\mathrm{p}) \varepsilon_r(\omega_\mathrm{s})} \right)^{1/2}, \tag{44}$$

we have an optical filling factor

$$\zeta = \left(1 + \frac{1}{\varepsilon_r(\omega_\mathrm{p})} \frac{\int_{S-S_\mathrm{wg}} |\mathbf{\Psi}_\mathrm{p}|^2 \,\mathrm{d}S}{\int_{S_\mathrm{wg}} |\mathbf{\Psi}_\mathrm{p}|^2 \,\mathrm{d}S} \right)^{-1} \tag{45}$$

that quantifies the fraction of optical energy propagating inside the nonlinear material S_wg ($\zeta \approx 1$ for a highly confined mode), relative to the total area (including the evanescent tail in $S - S_\mathrm{wg}$). The relative effective microwave mode area is given by

$$\Delta S = \int_S \varepsilon_r(\omega_\mathrm{m}) \left| \frac{\mathbf{\Psi}_\mathrm{m}}{\Psi_\mathrm{m0}} \right|^2 \mathrm{d}S, \tag{46}$$

where

$$\Psi_\mathrm{m0} = \frac{\int_{S_\mathrm{wg}} \Psi_\mathrm{m} |\Psi_\mathrm{p}|^2 \,\mathrm{d}S}{\int_{S_\mathrm{wg}} |\mathbf{\Psi}_\mathrm{p}|^2 \,\mathrm{d}S} \tag{47}$$

is the average microwave electric field inside the waveguide weighted by the optical mode profile. This effective field approximates the microwave field amplitude evaluated at the peak of the optical mode. While smaller CPW gaps minimize ΔS, they also degrade $Q_\mathrm{m,0}$, as well as the optical Q factors if the electrodes disturb the optical evanescent tails. Finally, the phase-matching term

$$I = \frac{1}{L} \int_0^L \hat{c}(\ell) \cdot \hat{z} u(\ell) e^{i \frac{\omega_\mathrm{m}}{v_\mathrm{g}} \ell} \,\mathrm{d}\ell \tag{48}$$

must be optimized by choosing an appropriate longitudinal microwave field distribution $u(\ell) = \frac{f(\ell)}{\sqrt{\int_0^L |f(\ell')|^2 \,\mathrm{d}\ell'}}$. The unit vector $\hat{c}$ is in the direction of the optical axis. The exponential term in Eq. (48) contains the group velocity v_g of the optical modes, and is a consequence of the first-order approximation $\beta_\mathrm{s} - \beta_\mathrm{p} \approx \omega_\mathrm{m} \left. \frac{\mathrm{d}\beta}{\mathrm{d}\omega} \right|_{\omega_\mathrm{p}} = \omega_\mathrm{m}/v_\mathrm{g}$. By convention, $f(\ell)$ is the microwave field component in the $\hat{z}$ direction. In this case, $\hat{c}$ can be a function of ℓ if the crystal is poled, and is always parallel (or anti-parallel) to $\hat{z}$. Since both optical modes have common polarization along the racetrack, no extra sign change is required. The total perimeter of the racetrack resonator is $L = 2\ell_s + 2\ell_b$.

For CPW even modes, the microwave field distribution is symmetric with respect to a plane (magnetic wall) perpendicular to the plane of the racetrack, parallel to its straight arms, and passing through its the center. This allows us to write Eq. (48) as

$$I = \frac{1}{L} \int_0^{\ell_s} u(\ell) e^{i \frac{\omega_\mathrm{m}}{v_\mathrm{g}} \ell} \,\mathrm{d}\ell \mp e^{i \frac{\omega_\mathrm{m}}{v_\mathrm{g}} (\ell_s + \ell_b)} \frac{1}{L} \int_0^{\ell_s} u(\ell_s - \ell) e^{i \frac{\omega_\mathrm{m}}{v_\mathrm{g}} \ell} \,\mathrm{d}\ell, \tag{49}$$

where we have assumed that the optical axis is uniform along each straight arm, but possibly different. Concretely, $\hat{c} = \hat{z}$ in the top arm, and $\hat{c} = \pm\hat{z}$ in the bottom arm. Taking the minus sign implies bilateral poling of the racetrack, which can be done by applying a high DC voltage to the CPW line terminated in open circuit. Then, we note that for the optical sidebands to be resonant,

$$\omega_\mathrm{m} = 2\pi M f_\mathrm{FSR} = 2\pi M \frac{v_\mathrm{g}}{L}, \tag{50}$$

where M is the integer number of optical FSRs between the two optical modes. Defining the integer $p = \mp e^{i \frac{\omega_m}{v_\mathrm{g}} \frac{L}{2}} = \mp e^{i\pi M}$, the racetrack factor $r = \ell_s/L$, the normalized wavenumber $\xi = 2\pi M r$, and applying a change of variables $x = \ell/\ell_s$ to scale the domain to $0 \leq x \leq 1$, we can rewrite Eq. (49) as

$$I = \sqrt{\frac{r}{2L}} \int_0^1 \frac{f(\ell_s x)}{\sqrt{\int_0^1 |f(\ell_s x)|^2 \, \mathrm{d}x}} g_p(x,\xi) \, \mathrm{d}x, \tag{51}$$

where,

$$g_p(x,\xi) = \begin{cases} 2e^{i\xi/2} \cos \xi(x-1/2), & p = 1 \\ i2e^{i\xi/2} \sin \xi(x-1/2), & p = -1 \end{cases}, \text{ and } \begin{array}{r|c|c} & M \text{ odd} & M \text{ even} \\ \hline \text{No poling} & p=1 & p=-1 \\ \text{Bilateral poling} & p=-1 & p=1. \end{array} \tag{52}$$

The overlap integral in Eq. (51) has the form of an inner product between a kernel $g_p(x,\xi)$, and a unity-norm field distribution. Therefore, the magnitude of I is maximum when $f(\ell_s x) = A g_p^*(x,\xi)$, where A is any constant. Various conclusions can be drawn from the above results:

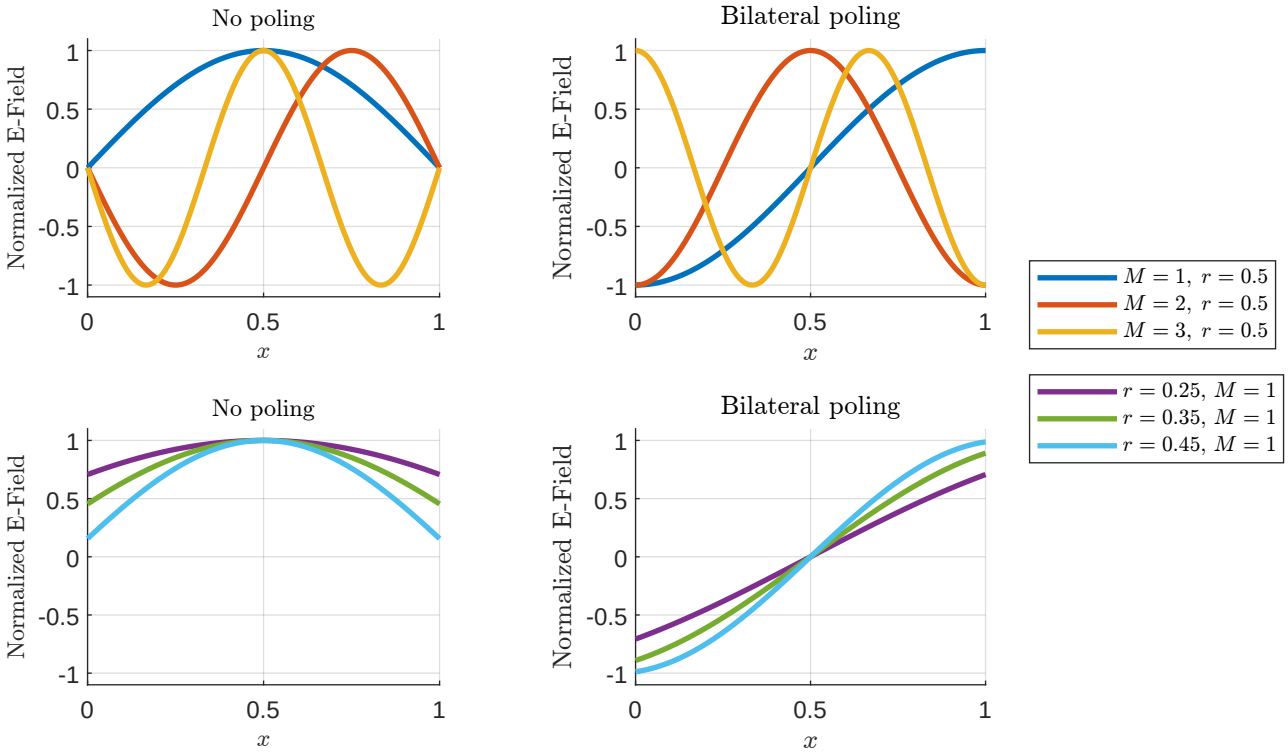

Figure S4. Optimal microwave field distributions $g_p(x,\xi)$ for different choices of parameters. In the top row, $r = 0.5$ is assumed for different values of M. In the bottom row, $M = 1$ is assumed for different values of r. A uniform (left column) and bilaterally poled (right column) optical axis is considered in each case

.

1. The kernel $g_p(x,\xi)$ is real-valued except for a global complex factor, for which a standing-wave distribution is optimal. In this case, the value of $|I|^2$ becomes

$$|I|^2_{\text{opt}} = \frac{r}{2L} \int_0^1 |g_p(x,\xi)|^2 \, \mathrm{d}x = \frac{r}{L} \left(1 + p \frac{\sin(\xi)}{\xi} \right). \tag{53}$$

2. The optimal standing-wave pattern satisfies $\beta_{\mathrm{m}} \ell_s = \xi = 2\pi M r$. From Eq. (50), we have $\beta_{\mathrm{m}} = \omega_{\mathrm{m}}/v_{\mathrm{p,m}} = 2\pi M v_{\mathrm{g}}/(L v_{\mathrm{p,m}})$. Therefore the optimal microwave phase velocity equals the optical group velocity $v_{\mathrm{p,m}} = v_{\mathrm{g}}$, as is the case for plane waves and whispering-gallery modes. This also implies that the optimal guided microwave wavelength $\lambda_{\mathrm{m}} = 2\pi/\beta_{\mathrm{m}} = L/M$ is fixed for a given optical waveguide and microwave frequency.

3. For a given M and optical group velocity, $L = M\lambda_\mathrm{m}$ is fixed, and $|I|^2_\mathrm{opt}$ increases with r. In practice, however, there exists a maximum $r < 1/2$, or a minimum ℓ_b, for which optical bending losses are not detrimental. One can more easily see this constraint by rewriting the racetrack factor as $r = 1/2 - \ell_b/L = 1/2 - \ell_b/(M\lambda_\mathrm{m})$.

4. A consequence of the point above is that choosing a higher M always results in a higher r for a given microwave frequency, since L increases while ℓ_b remains constant. However, for a sufficiently small $\ell_b/\lambda_\mathrm{m}$, $M = 1$ is still optimal because the increase in L has a greater effect on g_0 compared to r. The full effect can be seen in Fig. S5.

5. For an even CPW mode, the maximum value of $|I|^2 L$ is $1/2$, which occurs for the limiting case $r = 1/2$. For a phase-matched microwave whispering-gallery mode (i.e., $f(\ell) = \mathrm{sgn}(\ell_s - \ell)e^{-i\frac{\omega_\mathrm{m}}{v_g}\ell}$ with no crystal poling) the maximum value is $|I|^2 L = 2r = 1$ for $r = 1/2$ using Eq. (48). Therefore, more complex microwave structures that allow such non-CPW traveling-wave resonances could improve g_0 by a factor of $\sqrt{2}$ with respect to the optimal CPW case. Note that if only one of the two straight racetrack arms carried a microwave field (a slot line/ground-signal-type excitation) the optimal solution is again a phase-matched traveling wave, and $|I|^2 L = r/2$. A static solution $f(\ell) = 1$ yields $|I| \neq 0$ for $p = 1$ only, in which case $|I|^2 L = 2r\left(\frac{\sin \pi M r}{\pi M r}\right)^2$, which is always lower than Eq. (53).

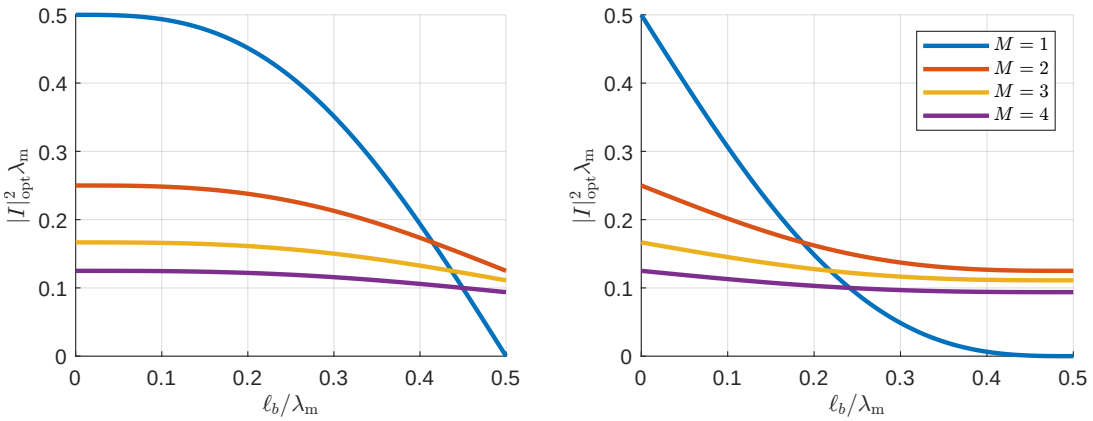

Figure S5. Maximum $|I|^2\lambda_\mathrm{m}$ versus optical bend length for different choices of M. **Left:** Uniform optical axis. **Right:** Bilaterally poled optical axis.

Figure S4 shows that the optimal field distribution is cosine-shaped when $p = +1$ (indicating a short-circuit-terminated resonator) and sine-shaped when $p = -1$ (indicating an open-circuit-terminated resonator). Note that while the value of $|I|^2 L$ for an unpoled, center-fed, half-wavelength, $M = 1$ resonator terminated in an open circuit is non-zero, the configuration is sub-optimal. Indeed, the field distribution has a $|\sin \xi(x - 1/2)|$ form, and for $r = 0.43$ (corresponding to the racetrack resonator measured in this work), Eq. (52) yields

$$|I|^2 L = \frac{r}{2}\frac{\left|\int_0^1 |\sin \xi(x-1/2)| 2e^{i\xi/2}\cos \xi(x-1/2)\,\mathrm{d}x\right|^2}{\int_0^1 |\sin \xi(x-1/2)|^2\,\mathrm{d}x} = 0.2537. \tag{54}$$

In contrast, for an optimal $\cos \xi(x - 1/2)$ distribution, obtainable with a half-wavelength resonator terminated in short circuit, $|I|^2 L = 0.4978$ as obtained from Eq. (53). This is a twofold improvement in cooperativity, or equivalently, a reduction by a factor of two in the microwave power requirement for achieving a given comb span. Note that if the open-circuit-terminated resonator were edge-fed instead of center-fed, the field pattern would become antisymmetric about $x = 1/2$, with the form $\sin \xi(x - 1/2)$, and $|I|^2 L = 0$, i.e., the vacuum coupling rate g_0 would vanish. This demonstrates the importance of using the correct topology.

In practice, there is also a trade-off between phase matching and the physical dimensions of the resonator. Since $r < 0.5$ for any practical design, the optimal microwave field distribution has a half-wavelength that is longer than ℓ_s. Thus, a phase-matched microwave resonator ($v_\mathrm{p,m} = v_\mathrm{g}$) will not fit the straight arm of the racetrack as evidenced from the cropped lobes in Fig. S4 (right). This can be circumvented in two ways: (i) by terminating the resonator in reactive loads using e.g., inductors or bridges to extend the resonator outside the racetrack, or (ii) by using slow-wave structures such that the half-wavelength fits inside the racetrack. The degradation produced by the latter approach on the value of the overlap integral will be small provided that $r \approx 0.5$. This is the strategy we employ for the present device, although the main motivation is to improve $Q_{\mathrm{m},0}$, as discussed in Section II B 3.

2. *Achieve critical coupling via impedance matching*

The resonant structure must be critically coupled to maximize the electric field enhancement inside the CPW resonator. Critical coupling is realized when the resonator impedance is matched with external microwave components, typically with a characteristic impedance (Z_0) of 50Ω. Minimization of microwave reflection is important for integration with high-power devices such as power amplifiers. A common strategy of impedance-matching a CPW resonator like the one employed in this work is to couple via a reactive element. This element, either in shunt or in series depending on the topology, serves as a matching network to the source impedance. However, such a network is designed for only a given microwave intrinsic Q factor, which may be *a priori* difficult to predict, leading to under-coupling or over-coupling. For simplicity, and to maintain design flexibility, we choose to feed these resonators with a ground-signal-ground (GSG) probe positioned off-centered. By adjusting the probe contact position along the CPW, it is possible to achieve critical coupling for a wide range of intrinsic quality factors.

To understand the microwave feeding scheme, consider a $L_{\mathrm{elec}} = \lambda/2$ transmission line resonator terminated in short circuits, as illustrated in Fig. S6a. Let ℓ_f be the distance between one end of the termination and the feeding position. In this configuration, the impedance seen by the source is the parallel combination of two short-circuited transmission lines with lengths ℓ_f and $L_{\mathrm{elec}} - \ell_f$. As ℓ_f is swept from $\ell_f = 0$ to $\ell_f = L_{\mathrm{elec}}/2$, the short line becomes longer and the long line becomes shorter. Therefore, as shown in Fig. S6b, the reflection coefficient seen towards the short side will start at the leftmost side of the Smith chart (a short circuit) and move clockwise in spiral form (non-constant circle due to non-zero losses) until $\ell_f = \lambda/4 = L_{\mathrm{elec}}/2$, at which point the reflection coefficient is the closest to an open circuit. Similarly, the reflection coefficient seen towards the long side will start at a short circuit (since it is $\lambda/2$ away from the short circuit termination) and move counter-clockwise around the Smith chart in spiral form until it is similarly closest to an open circuit. Since at any point on the line both reflection coefficients —and therefore impedances and admittances—are nearly complex conjugates of each other, their parallel equivalent is approximately purely resistive, with values that ideally range from $0\,\Omega$ (at the edge of the resonator) to $\infty\,\Omega$ (at the center of the resonator), encountering Z_0 somewhere in between.

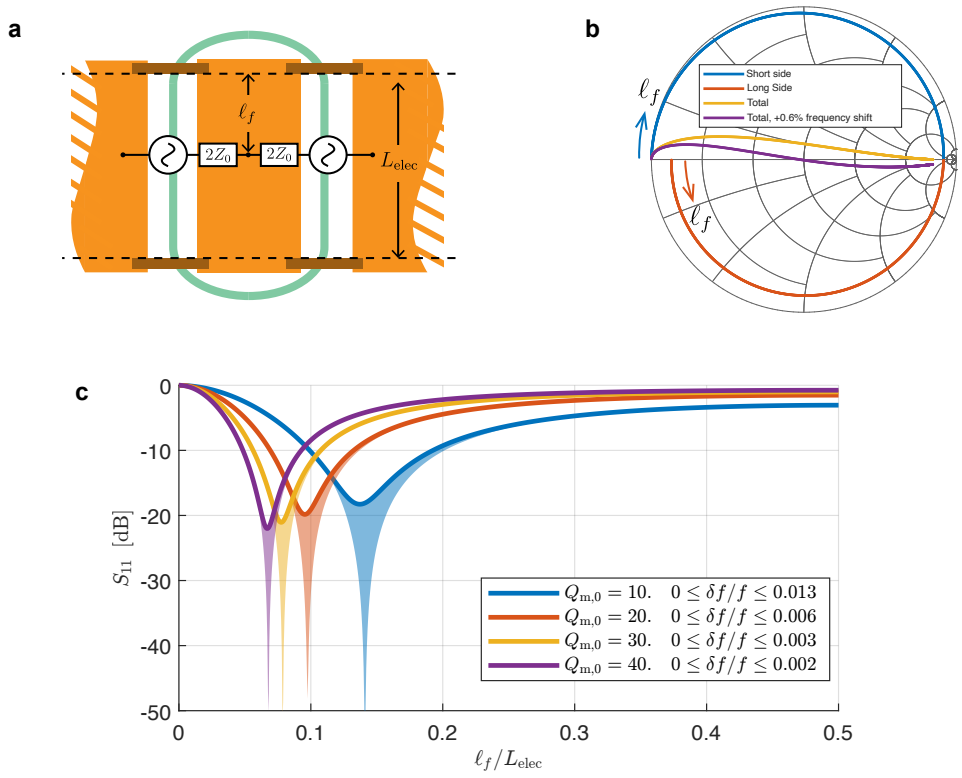

Figure S6. (a) Offset feeding schematic. (b) Smith chart representation of the reflection coefficients as ℓ_f is tuned. (c) Reflection coefficient of the resonator as a function of feeding position ℓ_f for different choices of intrinsic microwave $Q_{\mathrm{m},0}$.

If we consider a half-wavelength CPW resonator short-circuited on either end with characteristic impedance Z_{0l} and intrinsic quality factor $Q_{\mathrm{m},0}$, the achievable input resistance ranges from $0\,\Omega$ to $\frac{2}{\pi}Q_{\mathrm{m},0}Z_{0l}$. Therefore, it is possible in practice to match the resistive part of the input impedance to $50\,\Omega$ even for low microwave quality factors. The reactive part, however, does not cancel out perfectly for low-Q resonators due to the loss-induced asymmetry of the circle paths in Fig. S6b, resulting in the yellow path on the Smith chart. This effect is self-corrected with a slightly shifted resonance frequency $f + \delta f$. The shift

moves each reflection coefficient on its circular path in clockwise direction, but at different speeds (the longer side is faster) until complex conjugation is met. This is represented in the purple trace on Fig. S6b after a 0.6% frequency shift. In practice, the resonance frequency shift at which critical coupling occurs ranges between 0.2% and 1.3% of the nominal resonance frequency for microwave quality factors ranging from $Q_{\mathrm{m},0} = 10$ to $Q_{\mathrm{m},0} = 40$. This is shown in Fig. S6c where the solid lines delineate the reflection coefficient at the nominal frequency for different feeding positions, and the shaded region illustrates the improvement in impedance match with a frequency sweep $\delta f/f$. Here, the reflection coefficient is computed using the equations for the input impedances of two lossy transmission lines in parallel, each terminated with a short circuit:

$$Z_{\mathrm{in}}^{-1} = Z_{0l}^{-1} \coth \gamma \ell_f + Z_{0l}^{-1} \coth \gamma (L_{\mathrm{elec}} - \ell_f), \tag{55}$$

where γ and Z_{0l} are the propagation constant and characteristic impedance of the line. Note that our feeding strategy is also valid for open-terminated CPW resonators. However, care must be taken as the phase distribution of the mode varies significantly with the feed position, potentially leading to vanishing modal overlaps.

3. *Improve microwave intrinsic quality factor via periodic loading of CPW resonator*

We engineer the CPW resonator to optimize the product $|I|^2 Q_{\mathrm{m},0}$. We simulate an ungrounded CPW transmission line, with the layer stack composition (geometry) shown in Fig. S7a (Fig. S3), using finite-element method (FEM; Ansys HFSS) to extract the characteristic impedance Z_{0l} and propagation coefficient $\gamma = \alpha + i\beta$. The impedance of the excitation ports are de-embedded via ABCD matrices. The CPW electrode gap is chosen to be 6.5 µm to balance the trade-off between modulation efficiency and optical loss. The simulation yields $Q_{\mathrm{m},0} = \beta/(2\alpha) = 16.5$ and a microwave effective refractive index $n_{\mathrm{eff}} = c\beta/\omega_{\mathrm{m}} = 2.228$ at 29 GHz. The simulated n_{eff} is close to the optical group index, satisfying the phase matching requirement $\lambda_{\mathrm{m}} \approx L$ for $M = 1$. On the other hand, the microwave loss is significant and the electrodes would be too long to fit inside the (optical) racetrack resonator.

Consider a distributed circuit parameter model, where R', L', G' and C' denote the distributed series resistance, series inductance, shunt conductance, and shunt capacitance, respectively. At room temperature, the conductor Ohmic loss R' limits the $Q_{\mathrm{m},0}$ of narrow-gap CPWs. For $R' \ll \omega L$ and negligible dielectric loss $G' \to 0$, the propagation coefficient is approximately given by

$$\gamma = \alpha + i\beta = \sqrt{(R' + i\omega L')(G' + i\omega C')} \approx i\omega\sqrt{L'C'}\sqrt{1 - i\frac{R'}{\omega L'}} \approx \frac{R'}{2}\sqrt{\frac{C'}{L'}} + i\omega\sqrt{L'C'}. \tag{56}$$

The propagation loss $\alpha \propto 1/\sqrt{L'}$ and $Q_{\mathrm{m},0} \propto L'$ can therefore be improved by increasing the series distributed inductance of the narrow-gap CPW. Following the approach of [5], we load the line with a periodic series inductance as in Fig. S7b, synthesized from wide-gap (i.e., large characteristic impedance) short-circuit-terminated slot lines, or T-cells. In fact, the microstructure can also be interpreted as capacitive loading of the higher-Q *wide-gap* CPW line. In this case, although the microstructure increases $\alpha \propto \sqrt{C'}$, it does not affect the quality factor of the wide-gap transmission line. We therefore expect $Q_{\mathrm{m},0}$ of the periodically loaded line to be similar to that of the unloaded wide-gap CPW, with the additional advantage of higher field confinement. While periodic loading also introduces a slow-wave effect ($\beta \propto \sqrt{L'C'}$) that leads to a slight phase mismatch, the combined effect still results in a twofold cooperativity improvement, as summarized in Table I. Finally, the microstructure modifies the mode wavelength, allowing us to fit a full $\lambda/2$ resonator along the straight sections of the racetrack resonator.

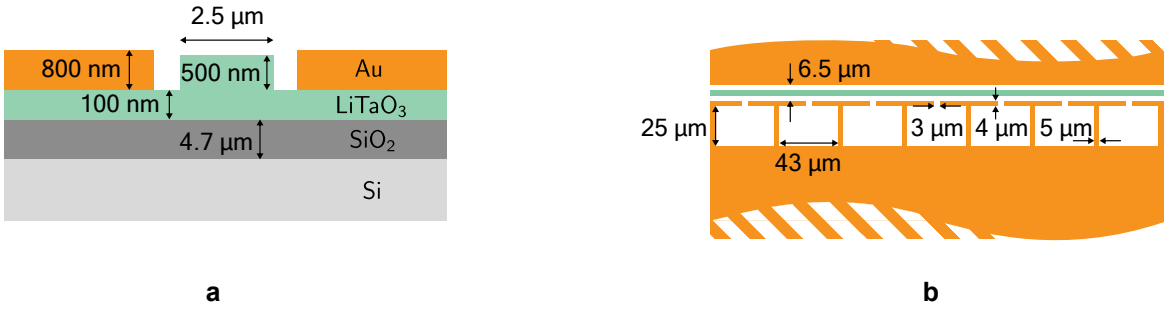

Figure S7. (a) Device layer stack composition (not to scale). (b) Geometry of periodic inductive loading to the narrow CPW line. Only half of the CPW structure is shown.

To extract the $Q_{\mathrm{m},0}$ from the measured and simulated S_{11} data, we bring the resonator to the critical coupling regime and measure the full width at half maximum. The measured $Q_{\mathrm{m},0} \approx 12.8$ deviates from the simulated $Q_{\mathrm{m},0} \approx 36.7$. Other methods

Transmission line	$\lvert I\rvert^2 L$	$Q_{\mathrm{m},0}$	n_{eff}	Figure of merit: $\lvert I\rvert^2 L Q_{\mathrm{m},0} \propto \mathcal{C}$
Standard CPW	0.5	16.5	2.228	8.25
Periodic loading	0.48	36.7	3.05	17.61

Table I. Summary of transmission line simulation results. Although the standard CPW has a better phase-matching overlap with the optical mode, the gain from Q by employing a loaded transmission line leads to a better overall design.

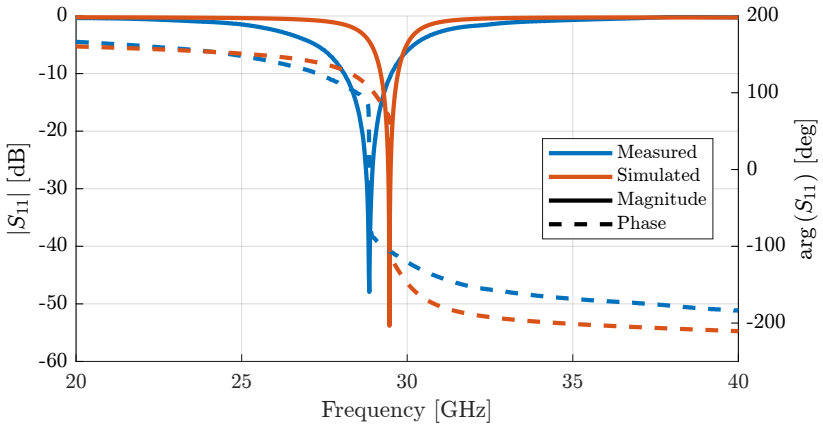

Figure S8. Measured and simulated S_{11} of the CPW resonator.

such as circle fitting on the Smith chart yield similar estimations. The significant Q reduction may be attributed to fabrication-induced and piezo-electric loss. Figure S8 compares the simulated and measured S_{11}. The difference in resonance frequency therein can be attributed to an underestimation of the $LiTaO_3$ dielectric constant in simulation.

C. Comparison between resonant and non-resonant implementations

While the theory above is useful for comparing different implementations of microwave resonators, a generalization to arbitrary microwave field distributions, whether resonant or not, is possible. Since $\sqrt{\mathcal{C}} \propto g = \sqrt{n_{\mathrm{m}}} g_0$, we can set $n_{\mathrm{m}} = W_{\mathrm{m}}/(\hbar\omega_{\mathrm{m}})$. As a result,

$$g = \sqrt{n_{\mathrm{m}}} g_0 = \frac{\varepsilon_0}{4}\sqrt{\frac{\omega_{\mathrm{p}}\omega_{\mathrm{s}}}{W_{\mathrm{p}}W_{\mathrm{s}}}}\int_{\mathrm{LiTaO_3}} \chi^{(2)}_{ijk} E_{\mathrm{p},i} E^*_{\mathrm{s},j} E_{\mathrm{m},k}\,\mathrm{d}V \approx \frac{\chi^{(2)}_{333}\omega_{\mathrm{p}}\zeta}{2\varepsilon_r(\omega_{\mathrm{p}})}\lvert E\rvert_{\mathrm{peak}}\Lambda, \tag{57}$$

where $\Lambda = |I|\sqrt{\int_0^L |f(\ell)|^2\,\mathrm{d}\ell}$. By convention, we have normalized $f(\ell)$ such that $\max[f(\ell)] = 1$, and $|\Psi_{\mathrm{m}0}| = \lvert E\rvert_{\mathrm{peak}} \propto \sqrt{P_{\mathrm{m}}}$ is the peak electric field along the resonator, inside the optical waveguide. Higher values of $\lvert E\rvert_{\mathrm{peak}}$ are achieved with higher-Q microwave resonators that are critically coupled. Equation (57) allows us to compute g from the peak microwave electric field and its geometric distribution along the optical waveguide obtained from driven full-wave simulations excited with available power P_{m}. The factor Λ is purely geometrical, with $\Lambda = |I|\sqrt{L_{\mathrm{elec}}}$ for a (multiple of) half-wavelength standing wave, with $\Lambda \to 1/2$ in the limiting case where $r \to 1/2$.

Let us compare the performance of the two microwave structures presented in this work, namely, the offset-fed inductively-loaded half-wavelength resonator terminated in short circuits (Fig. S9a), and the center-fed non-resonant pair of 50 µm wide coplanar-strip (CPS) transmission lines terminated in open circuits (Fig. S9b). Figure S9c and Fig. S9d show the field distributions in both structures at 29.6 GHz obtained from 3D FEM simulations made in Ansys HFSS, normalized to the square root of the available power. It is possible to find analytical expressions for the fields in a transmission line of characteristic impedance Z_{0l} terminated with reflection coefficients Γ_{L}. The line is fed at an arbitrary distance ℓ_f from one end by a voltage source with internal real-valued impedance Z_0 (or a line with characteristic impedance Z_0). Referring to Fig. S9e, the voltage distribution becomes

$$v(d_1) = \begin{cases} v_1^+\left(e^{\gamma d_1} + \Gamma_{\mathrm{L}} e^{-\gamma d_1}\right) & d_1 \le \ell_f \\ v_2^+\left[e^{\gamma(L_{\mathrm{elec}}-d_1)} + \Gamma_{\mathrm{L}} e^{-\gamma(L_{\mathrm{elec}}-d_1)}\right] & d_1 \ge \ell_f \end{cases}. \tag{58}$$

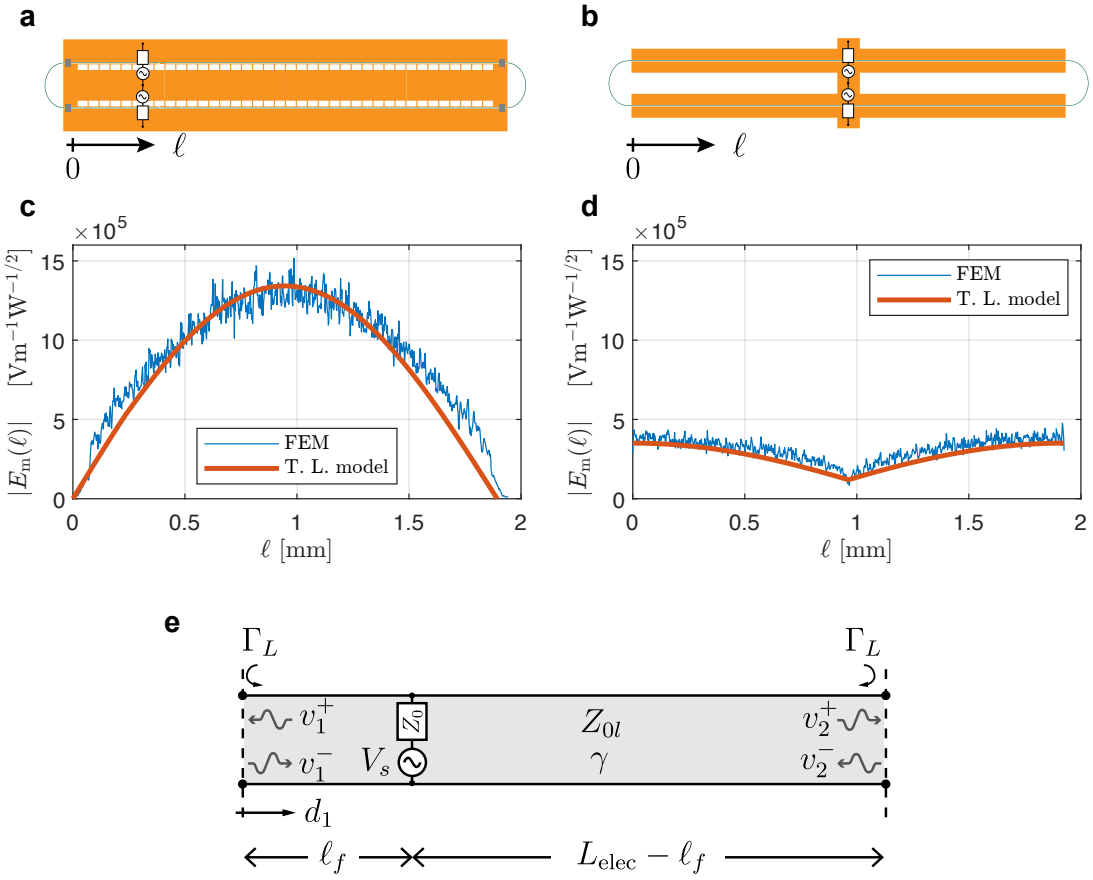

Figure S9. Layout of optical racetrack resonator embedded in microwave resonator (a) and non-resonant electrodes (b). The electric field distribution in resonant and non-resonant topologies is shown in (c) and (d), respectively, and is obtained from the theoretical transmission line model, and compared with FEM simulations. Panel (e) depicts the schematic of the transmission line model.

The boundary condition at the feed point entirely determines v_1^+ and v_2^+ through the double equation

$$v_1^+\left(e^{\gamma\ell_f}+\Gamma_{\rm L}e^{-\gamma\ell_f}\right)=v_2^+\left[e^{\gamma(L_{\rm elec}-\ell_f)}+\Gamma_{\rm L}e^{-\gamma(L_{\rm elec}-\ell_f)}\right]=\frac{Z_{\rm in}}{Z_{\rm in}+Z_0}V_s, \tag{59}$$

where

$$Z_{\rm in}=Z_{0l}\left[\frac{1-\Gamma_{\rm L}e^{-2\gamma\ell_f}}{1+\Gamma_{\rm L}e^{-2\gamma\ell_f}}+\frac{1-\Gamma_{\rm L}e^{-2\gamma(L_{\rm elec}-\ell_f)}}{1+\Gamma_{\rm L}e^{-2\gamma(L_{\rm elec}-\ell_f)}}\right]^{-1}, \tag{60}$$

and

$$|V_{\rm s}|=\sqrt{8Z_0P_{\rm m}}. \tag{61}$$

The voltage in Eq. (58) is then converted to electric field via 2D FEM simulations of the quasi-TEM mode. Such 2D simulations also provide values for γ and Z_{0l}. The transmission line model predicts reasonably well the field distribution along the transmission line for resonant and non-resonant structures when compared to the 3D full-wave FEM simulations as shown in Fig. S9c and Fig. S9d. In Fig. S10, the maximum peak electric fields as a function of frequency, obtained through the transmission line model and FEM simulations are compared. Three cases are studied: the non-resonant open-terminated transmission line and the short-terminated resonator exhibiting intrinsic quality factors $Q_{\rm m,0}=36.7$ (expected) and $Q_{\rm m,0}=12.8$ (measured). The latter case is modeled in Ansys HFSS by artificially introducing a conductive sheet of resistivity $14\,{\rm k}\Omega/\square$ at the silicon-oxide interface. Figure S11 shows good agreement between the geometric factors of the field profile obtained from the transmission line model and the FEM simulation. From these results, we can estimate g for a given available microwave power $P_{\rm m}$ using Eq. (57), shown in Fig. S12 for resonant and non-resonant cases for $P_{\rm m}=7\,{\rm dBm}$. In this case, we estimate $g\approx 2\pi\times 290.46\,{\rm MHz}$ for the resonator with $Q_{\rm m,0}=12.8$.

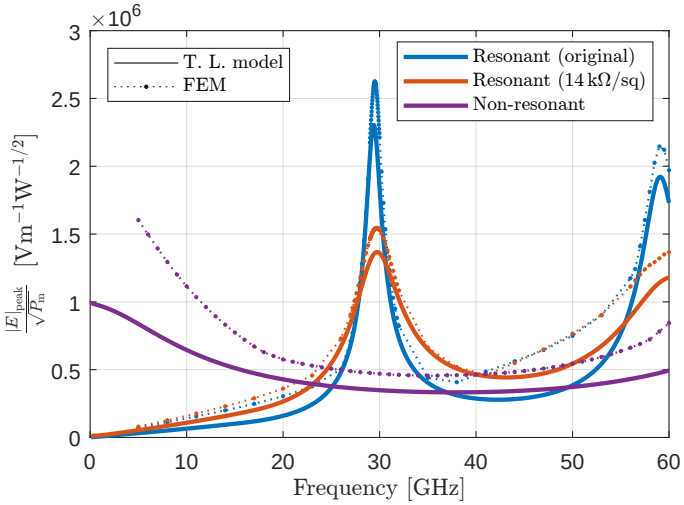

Figure S10. Maximum peak electric field $|E|_{\mathrm{peak}}$ per square root of available input microwave power inside resonant and non-resonant structures as a function of frequency.

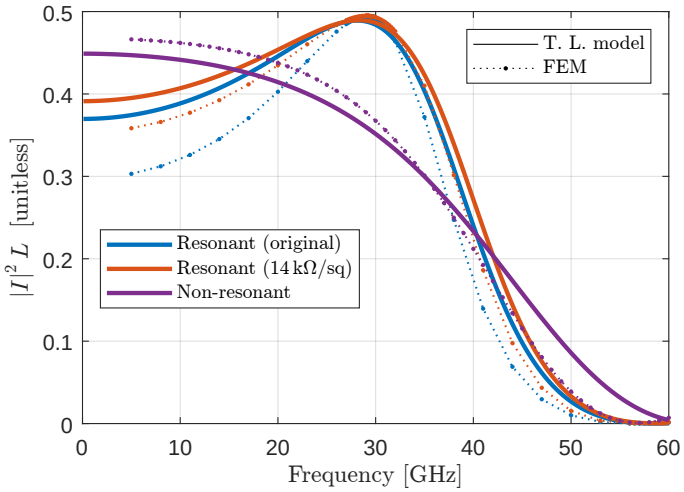

Figure S11. Phase-matching geometric factor $|I|^2 L$ as a function of frequency for resonant and non-resonant structures, calculated with the transmission line model and through FEM simulations. Note that the non-resonant open-circuited transmission line becomes resonant at $\sim 40\,\mathrm{GHz}$, at which point $|I|^2 L \approx 0.25$.

In accordance with Section I B, the effective coupling rate g is experimentally measured via two independent methods. First, we fit the power ratio between consecutive comb lines to the cooperativity as a function of microwave power levels, as in Section I C. Second, we measure the optical spectrum for different microwave power levels and extract g from the optical mode splittings [6]. Both methods provide consistent values of g as shown in Fig. S13a. We can then estimate $n_{\mathrm{m}} = P_{\mathrm{m}} Q_{\mathrm{m},0}/(\hbar\omega_{\mathrm{m}}^2)$ for a critically coupled resonator, resulting in the estimations of g_0 shown in Fig. S13b. Here, we obtain $g_0/(2\pi) = (2.31 \pm 0.29)\,\mathrm{kHz}$ from slope measurements and $g_0/(2\pi) = (2.03 \pm 0.47)\,\mathrm{kHz}$ from mode splitting measurements, where the quoted uncertainty corresponds to two standard deviations. By extracting the proportionality constant $g/\sqrt{P_{\mathrm{m}}} \propto g_0$ via a single-parameter exponential fit of the measurement data in Fig. S13a, we obtain $g_0/(2\pi) = (2.22 \pm 0.04)\,\mathrm{kHz}$ from slope measurements and $g_0/(2\pi) = (2.19 \pm 0.18)\,\mathrm{kHz}$ from mode splitting measurements, where the quoted uncertainty corresponds to the 95% confidence interval of the fit. From simulations and the transmission line model, we obtain $g_0/(2\pi) = 2.20\,\mathrm{kHz}$.

III. DISPERSION-ENGINEERED LITHIUM TANTALATE WAVEGUIDES

In optical resonators, the integrated dispersion $D_{\mathrm{int}}(\mu)$ at the μ^{th} longitudinal mode from the input carrier is defined by

$$\omega(\mu) = \omega_0 + D_1\mu + D_{\mathrm{int}}(\mu), \tag{62}$$

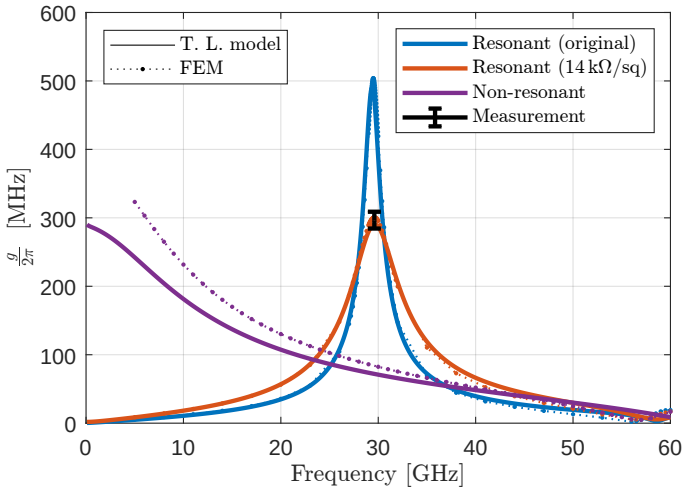

Figure S12. Nonlinear coupling rate g for a microwave available power $P_{\mathrm{m}} = 7\,\mathrm{dBm}$ estimated with transmission line model and with FEM simulations. The measured value of g in the resonator is included. The error bar corresponds to two standard deviations of a sample that comprises seven microwave power levels for the determination of g by means of the comb slope.

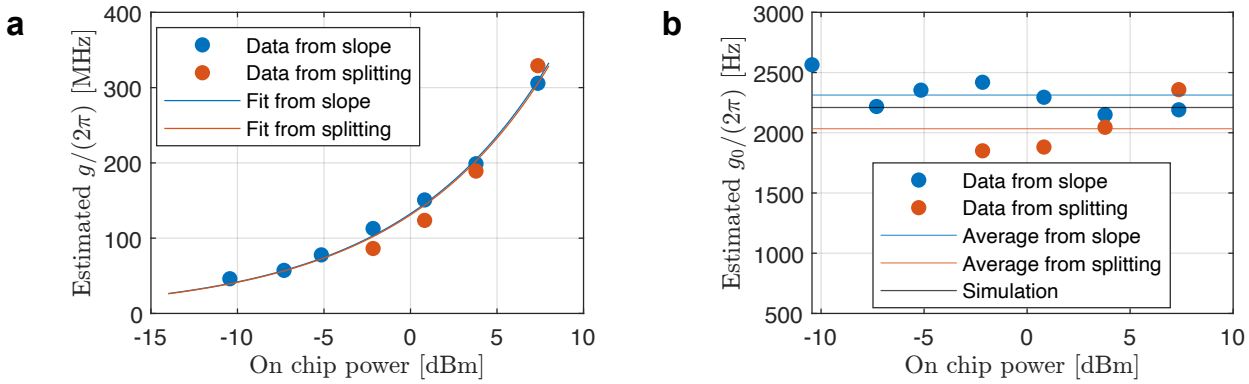

Figure S13. (a) Measurement of the nonlinear coupling rate g via the cooperativity $\sqrt{C}$ obtained through the power ratio between consecutive lines of measured comb spectra for different microwave power levels. The lines are single-parameter exponential fits to $g = Ae^{\frac{\ln(10)}{20}P_{\mathrm{m,dBm}}}$. (b) Estimation of the vacuum nonlinear coupling rate $g_0 = g/\sqrt{n_{\mathrm{m}}}$.

where $D_1 = \omega_{\mathrm{FSR}}$ is the optical FSR. The integrated dispersion D_{int} can be expanded as

$$D_{\mathrm{int}}(\mu) = \frac{1}{2!}D_2\mu^2 + \frac{1}{3!}D_3\mu^3 + \frac{1}{4!}D_4\mu^4 + ... \tag{63}$$

To generate an EO comb, the dispersion must fall within the comb existence range such that $|D_{\mathrm{int}}| < 2g$. Consequently, dispersion engineering is essential for ultra-broadband comb generation. A unique advantage of integrated photonic waveguides is the engineering degrees of freedom they offer to tailor the dispersion profile. In deeply etched photonic waveguides, specifically those used in our work with a 600-nm total thickness (100-nm slab and 500-nm etch depth), the dispersion profile can be precisely engineered by adjusting the waveguide width. This adjustment modifies the D_2 and D_4 parameters, allowing them to cancel each other to achieve a flat dispersion.

IV. OPTICAL MICRORESONATOR CHARACTERIZATION

The characterization results of the racetrack microresonators used in the experiment are summarized in Fig. S15. Device **C4_R202** (**C11_R102**) corresponds to the design with resonant (non-resonant) electrodes in Fig. 3i, generating a 450-nm (100-nm) comb. Device **C2_R104**, employed in Fig. 3h, also has resonant electrodes. In particular, it is under-coupled, resulting in lower comb generation efficiency compared to the over-coupled ones despite a narrower total linewidth. This characteristic is desirable for low microwave power-driven comb generation, enabling a 100-nm comb with only 13 dBm of microwave

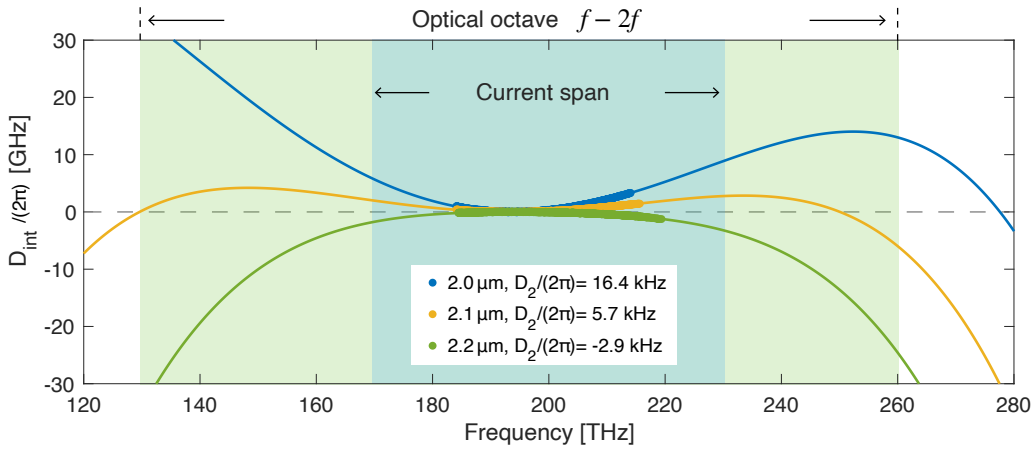

Figure S14. Measured integrated dispersion $D_{\rm int}/(2\pi)$ for x-cut $LiTaO_3$ waveguide with a total thickness of 600 nm (100-nm slab and 500-nm etch depth), with different waveguide widths.

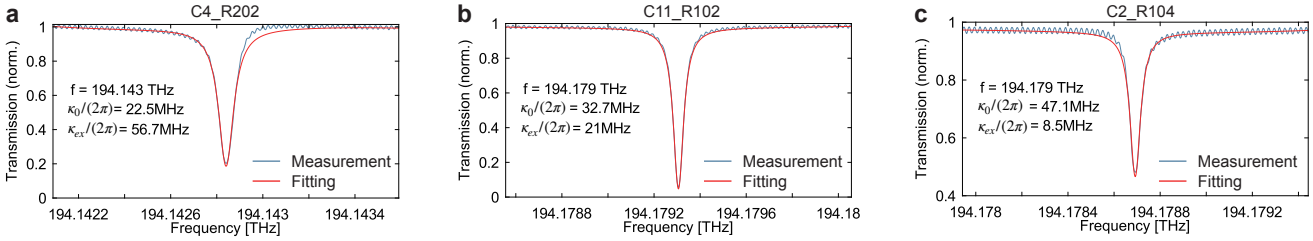

Figure S15. The microresonator resonances used for comb generation. The intrinsic loss rate and external coupling rate are denoted as κ_0 and $\kappa_{\rm ex}$, respectively.

pump. All the devices have an optical FSR of around 29.6 GHz with slight variations. In the experiments, the microwave pump frequencies are optimized for each device to match the corresponding optical FSR.

V. SELF-INJECTION LOCKING AND HYBRID INTEGRATION

A. Noise reduction in self-injection locking

In our system, the comb laser source is a hybrid-integrated distributed feedback (DFB) semiconductor laser diode. As shown in Fig. S16, the free-running DFB laser exhibits significant frequency noise. However, when the DFB laser diode is butt-coupled to the comb generator chip, self-injection locking occurs, resulting in a frequency noise reduction of more than 10 dB. Self-injection locking involves an external low-loss cavity, where some amount of light is reflected back into the laser via resonant Rayleigh scattering, affording optical feedback to the laser. Consequently, the laser's linewidth and frequency noise are proportionally reduced, and the reduction is determined by the square of the quality factor of the external resonator $Q_{\rm res}$[7, 8]. The ultimate limit of this noise reduction would be constrained by the fundamental refractive noise [9]. In our system, a distributed feedback laser (DFB) is self-injection-locked to the racetrack microresonator, also used for comb generation. To prevent lock instability, the reflection is provided by only random Rayleigh backscattering from material and fabrication defects in the photonic waveguides and not enhanced by additional reflector structures. The frequency noise reduction factor can be expressed as [10]

$$\frac{\delta f}{\delta f_{\rm free}} \approx \frac{Q_{\rm d}^2}{Q_{\rm res}^2}\frac{1}{16\Gamma_{\rm res}^2(1+\alpha_g^2)} \propto \frac{1}{Q_{\rm res}^2}, \tag{64}$$

where δf_{free} represents the frequency fluctuation of the DFB laser due to drive current noise and temperature fluctuations and δf is the frequency deviation of the locked laser. The quality factors of the DFB laser diode and the microresonator are denoted as $Q_{\rm d} \sim 10^3$–10^4 and $Q_{\rm res} \sim 10^6$–10^7. $\Gamma_{\rm res}$ is the resonant amplitude reflection coefficient from the microresonator, and α_g is the phase-amplitude coupling factor, which is approximately unity.

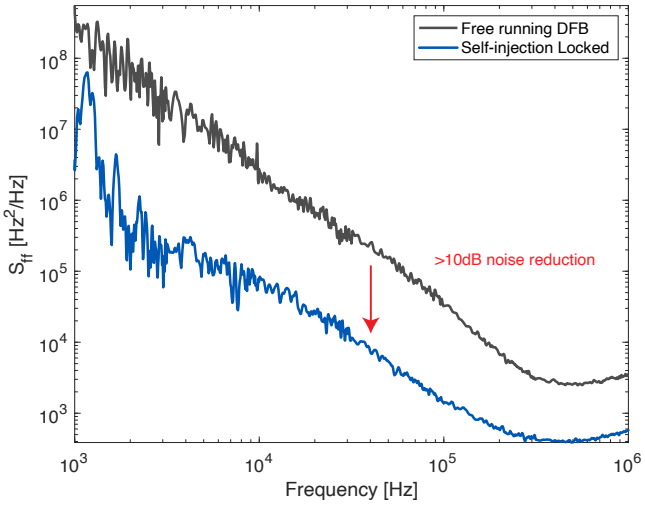

Figure S16. Laser frequency noise of a free-running distributed feedback laser diode (DFB) and when it is self-injection-locked with the $LiTaO_3$ resonator, measured using heterodyne detection with a reference laser.

B. Self-injection locking during electro-optic comb generation

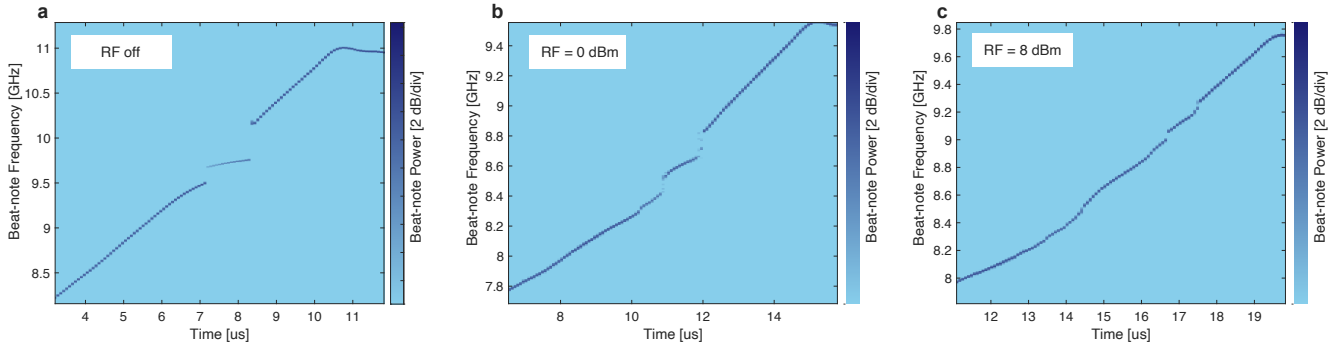

Figure S17. Time-frequency spectrogram of the input carrier mode beat with a reference laser, with different microwave powers applied for comb generation. The microwave frequency matches the optical free spectral range.

The significant linewidth reduction due to self-injection locking provides a unique advantage for hybrid-integrated comb generators, as low phase noise is essential for many applications. The detuning range $\Delta f_{\rm lock}$ where self-injection locking can occur depends on the sharpness of the frequency-dependent reflection peak (cavity linewidth of the $LiTaO_3$ cavity) and the strength of the optical reflection [10], given by

$$\frac{\Delta f_{\rm lock}}{f} \approx \sqrt{1+\alpha_g^2}\frac{\Gamma_{\rm res}}{Q_{\rm d}}. \tag{65}$$

Figure S17 shows the measured time-frequency spectrogram of the beating between the input carrier mode of the comb and a stable reference laser. Frequency pulling corresponding to self-injection locking can be seen in Fig. S17a and S17b, without and with a weak microwave pump. The optical mode splitting induced by the microwave drive is also observed in Fig. S17b, as the frequency pulling range is split into two. As the microwave pump increases further in Fig. S17c, no frequency pulling, and thus no self-injection locking, is observed. This is due to the reduced reflection $\Gamma_{\rm res}$ of the split resonances caused by the applied microwave tone. In summary, we found that although self-injection locking can coexist with low microwave pump power (narrow comb), the current single-microresonator configuration cannot support the generation of an ultra-broadband EO comb and self-injection locking simultaneously. Alternative designs, such as dual-ring comb generation [11] or adding a separate extended distributed Bragg reflector (E-DBR) section [12], may be required.

VI. DEVICE FABRICATION

The devices were fabricated on x-cut single crystalline thin-film $LiTaO_3$ wafers from SIMIT-Shanghai. The thin-film $LiTaO_3$ wafers were fabricated by ion-cutting and wafer bonding methods. Commercially available optical-grade bulk $LiTaO_3$ were used. Hydrogen ions with an energy of 100 keV and a fluence of 7.0e16 cm^{-2} were implanted into a 4-inch x-cut bulk $LiTaO_3$ wafer, creating an ion-damaged layer beneath the surface. The implanted wafer was then inverted and bonded to a 525 µm thick high-resistivity silicon carrier wafer coated with 4.7 µm thick thermal silicon dioxide. A thermal annealing process 190 °C was applied, allowing the separation of the remaining bulk wafer and the exfoliated $LiTaO_3$ thin film. Subsequently, we carried out edge removal of the $LiTaO_3$ thin film and performed chemical mechanical polishing to eliminate the rough and defect-laden layer of $LiTaO_3$ impacted by H-ion implantation, reducing the $LiTaO_3$ film to the target thickness of 600 nm. The wafer stack consists of a 600 nm thin-film $LiTaO_3$, a 4.7 µm thick thermal silicon dioxide, and a 525 µm thick high-resistivity silicon carrier wafer. The $LiTaO_3$ photonics integrated circuits were fabricated using the diamond-like-carbon (DLC) hard mask, which we recently demonstrated for both LNOI and LTOI platforms [13, 14]. We employed deep-ultraviolet (DUV) stepper photolithography (ASML PAS 5500/350C) to define the photonic waveguides and components. The pattern was transferred into the DLC hard mask layer through oxygen-based dry etching in a reactive ion etcher. Then, the patterns were transferred to the $LiTaO_3$ layer using ion-beam etching (Veeco Nexus IBE350). Additional chemical cleaning is used to remove the amorphous redeposition of $LiTaO_3$ during the ion-beam etching process. The etch depth is 500 nm, leaving a 100 nm thick slab for dispersion engineering. The metal layer was patterned with the same DUV tool and fabricated using a lift-off process with silicon dioxide as a sacrificial layer. The silicon dioxide sacrificial layer is removed in buffered oxide etchant after electrode fabrication. The metallization layer consists of a 20-nm aluminum adhesion layer and an 800-nm gold layer to reduce Ohmic loss and enhance the microwave quality factor. After electrode fabrication, 800 nm thick aluminum air bridges were fabricated using a photoresist-based lift-off process (AZ NLOF 2020), with the bridge curvature defined by thermal reflow [15]. The minimum distance between the air bridges and the photonic waveguide is maintained at more than 1.5 µm to prevent additional optical loss. Chip singulation is achieved through a combination of dry etching for the $LiTaO_3$ and wet oxide layers using fluoride chemistry, as well as deep reactive-ion etching (DRIE) for the silicon carrier [16]. The process ensures smooth facets for butt coupling with the DFB laser diode. The residual photoresists are removed using TechniStrip NI555 and cleaned with oxygen plasma.

[1] Bethe, H. A. & Schwinger, J. *Perturbation Theory for Cavities*. No. D1-117 in National Defense Research Committee, Contractor's Report, Cornell University (Massachusetts Institute of Technology, Radiation Laboratory, Cambridge, Mass., 1943).

[2] Tsang, M. Cavity quantum electro-optics. *Physical Review A* **81**, 063837 (2010).

[3] Javerzac-Galy, C. *et al.* On-chip microwave-to-optical quantum coherent converter based on a superconducting resonator coupled to an electro-optic microresonator. *Physical Review A* **94**, 053815 (2016).

[4] Han, X. *et al.* Microwave-optical quantum frequency conversion. *Optica* **8**, 1050–1064 (2021).

[5] Kharel, P., Reimer, C., Luke, K., He, L. & Zhang, M. Breaking voltage–bandwidth limits in integrated lithium niobate modulators using micro-structured electrodes. *Optica* **8**, 357–363 (2021). URL https://doi.org/10.1364/OPTICA.416155.

[6] Rueda, A., Sedlmeir, F., Kumari, M., Leuchs, G. & Schwefel, H. G. Resonant electro-optic frequency comb. *Nature* **568**, 378–381 (2019). URL https://doi.org/10.1038/s41586-019-1110-x.

[7] Laurent, P., Clairon, A. & Breant, C. Frequency noise analysis of optically self-locked diode lasers. *IEEE Journal of Quantum Electronics* **25**, 1131–1142 (1989).

[8] Spano, P., Piazzolla, S. & Tamburrini, M. Theory of noise in semiconductor lasers in the presence of optical feedback. *IEEE journal of quantum electronics* **20**, 350–357 (1984).

[9] Zhang, J. *et al.* Fundamental charge noise in electro-optic photonic integrated circuits. *arXiv preprint arXiv:2308.15404* (2023).

[10] Kondratiev, N. *et al.* Self-injection locking of a laser diode to a high-q wgm microresonator. *Optics Express* **25**, 28167–28178 (2017).

[11] Hu, Y. *et al.* High-efficiency and broadband on-chip electro-optic frequency comb generators. *Nature photonics* **16**, 679–685 (2022). URL https://doi.org/10.1038/s41566-022-01059-y.

[12] Siddharth, A. *et al.* Hertz-linewidth and frequency-agile photonic integrated extended-dbr lasers. *arXiv preprint arXiv:2306.03184* (2023).

[13] Wang, C. *et al.* Lithium tantalate photonic integrated circuits for volume manufacturing. *Nature* **629**, 784–790 (2024).

[14] Li, Z. *et al.* High density lithium niobate photonic integrated circuits. *Nature Communications* **14**, 4856 (2023).

[15] Snigirev, V., Kono, S., Wang, R. N. & Blésin, T. *Fabrication of aluminium airbridges for microwave interconnects on lithium niobate on Damascene silicon nitride photonic chips* (2022). URL https://zenodo.org/record/7221147.

[16] Liu, J. *Separating a wafer into chips using dry etching and backside grinding* (2021). URL https://zenodo.org/record/5145993.